


Room-temperature X-ray powder diffraction data for bosentan monohydrate

Robert A. Toro¹ , Analio J. Dugarte-Dugarte² , José A. Henao¹ , Graciela Díaz de Delgado²  and José M. Delgado² 

¹*Grupo de Investigación en Química Estructural (GIQUE), Escuela de Química, Facultad de Ciencias, Universidad Industrial de Santander, Bucaramanga, Colombia*

²*Laboratorio de Cristalografía-LNDRX, Departamento de Química, Facultad de Ciencias, Universidad de los Andes, Mérida, Venezuela*

(Received 20 September 2024; revised 01 January 2025; accepted 09 January 2025)

Abstract: The room-temperature X-ray powder diffraction data for bosentan monohydrate, an API used in the treatment of pulmonary arterial hypertension, is presented. Bosentan monohydrate is monoclinic, $P2_1/c$ (No. 14), with unit cell parameters $a = 12.4520(7)$ Å, $b = 15.110(1)$ Å, $c = 15.0849(9)$ Å, $\beta = 95.119(5)^\circ$, $V = 2827.0(3)$ Å³, $Z = 4$. All the diffraction maxima recorded were indexed and are consistent with the $P2_1/c$ space group. The crystal structure of this material corresponds to the phase associated with Cambridge Structural Database entry NEQHEY, which was determined at 123 K. The successful Rietveld refinement, carried out with TOPAS-Academic, showed the single-phase nature of the material and the good quality of the data. A comprehensive analysis of intra- and intermolecular interactions corroborates that the structure is dominated by extensive hydrogen bonding, accompanied by C–H $\cdots\pi$ and $\pi\cdots\pi$ interactions. Hirshfeld surface analysis and fingerprint plots indicate that the most important interactions are H \cdots H and O \cdots H/H \cdots O in bosentan and the water molecule and C \cdots H/H \cdots C interactions in bosentan.

© The Author(s), 2025. Published by Cambridge University Press on behalf of International Center for Diffraction Data. This is an Open Access article, distributed under the terms of the Creative Commons Attribution licence (<http://creativecommons.org/licenses/by/4.0>), which permits unrestricted re-use, distribution and reproduction, provided the original article is properly cited. [doi:10.1017/S0885715625000065]

Key words: bosentan monohydrate, hydrogen bonding, powder diffraction data, room temperature, Rietveld refinement, pulmonary arterial hypertension

I. INTRODUCTION

Bosentan (4-tert-butyl-*N*-[6-(2-hydroxyethoxy)-5-(2-methoxyphenoxy)-2,2'-bipyrimidin-4-yl]benzenesulfonamide, C₂₇H₂₉N₅O₆S; [Figure 1](#)) is a nonpeptide pyrimidine derivative approved by the FDA for the treatment of pulmonary arterial hypertension (PAH), when high blood pressure develops in the pulmonary arteries that carry oxygen-poor blood from the heart to the lungs (Enevoldsen et al., 2020). Bosentan is sold under the brand names Tracleer®, Safebo®, and others. It was the first endothelin-I receptor antagonist approved for the treatment of PAH, in 2001, with World Health Organization (WHO) functional classes III–IV (Mathier and Ishizawar, 2010; Enevoldsen et al., 2020). The WHO divides pulmonary hypertension into five groups, I–V, based on its cause. Bosentan decreases both pulmonary vascular resistance and systemic vascular resistance, increasing cardiac output without increasing the heart rate. Therefore, it is an important therapeutic option.

A search in the Cambridge Structural Database (CSD), version 2024.1.0 (Groom et al., 2016), led to five reports with crystal structures related to bosentan. Three of them were for the bosentan monohydrate phase, BSN·H₂O (Refcodes NEQHEY,

Kaur et al., 2013; NEQHEY01, Trzcińska et al., 2016; NEQHEY02, Łaszcz et al., 2012). The structure determinations reported in those entries were carried out at 123 and 100 K. The two additional reports found were a cocrystal phase with succinic acid (Refcode DEGPEO, Barbas et al., 2022) and a zinc complex (Refcode NAMGIU, Khandar et al., 2017). Barbas and coworkers also prepared two new cocrystal phases with resorcinol and 4-hydroxybenzoic acid, respectively, reporting the X-ray powder diffraction patterns, the space group, and the unit cell parameters. The report found in the ICDD PDF-5+ Database (Kabekkodu et al., 2024) contains the powder diffraction pattern of bosentan monohydrate (PDF 05-006-0054) calculated using the crystal structure data at 123 K reported for NEQHEY (Kaur et al., 2013).

After searching for “Bosentan monohydrate” on the Google Patents site (<https://patents.google.com>), many entries are encountered. Some of them refer to the preparation of BSN·H₂O and various forms of sodium and potassium derivatives. Only in one of the patents (Sidoryk et al., 2014), the unit cell parameters of a BSN·H₂O phase are reported. This phase corresponds to the phase reported in the CSD under the Refcodes NEQHEY01 (Trzcińska et al., 2016) and NEQHEY02 (Łaszcz et al., 2012).

Several studies associated with the characterization of bosentan monohydrate have been published in the open

Corresponding author: Graciela Díaz de Delgado; Email: gdiazdedelgado@gmail.com



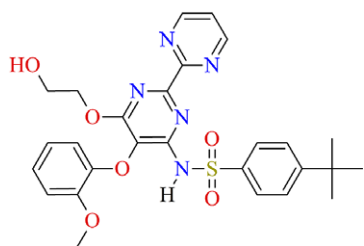


Figure 1. Molecular diagram of bosentan.

literature. Some of them involve the preparation and characterization of microparticles (Lee et al., 2016), inclusion complexes (Jadhav and Pore, 2017), and nanoparticles (Giménez et al., 2019; Mohapatra et al., 2022). There are also reports of one intermediate (Sagar et al., 2016) and various derivatives of bosentan (Easwaramoorthi et al., 2015). The amorphization of crystalline bosentan monohydrate has been studied by Minecka et al. (2022). They prepared an amorphous phase by vitrification and cryomilling. The resulting phase was characterized by X-ray powder diffraction, thermogravimetry, differential scanning calorimetry, Fourier-transformed infrared spectroscopy, and broad-band dielectric spectroscopy (Minecka et al., 2022). The processes of dehydration and amorphization of this drug were also followed by diffraction, thermal, and spectroscopic techniques and by saturation solubility and dissolution studies (Krupa et al., 2022). The unindexed powder diffraction plot reported by these authors cannot be used to properly identify the monohydrate phase of bosentan in a phase ID process because the powder diffraction data are not included in this publication.

In the last few years, several compounds of pharmaceutical interest have been studied in our laboratory (Dugarte-Dugarte et al., 2023; Toro et al., 2022; Dugarte-Dugarte et al., 2022; Dávila-Miliani et al., 2020). Because no powder diffraction pattern for bosentan monohydrate at room temperature has been included in the PDF-5+ database and the crystal structure of this material was determined at 100 and 123 K, for identification purposes at ambient conditions, it was decided to record and analyze the powder diffraction pattern at

ambient temperature for inclusion in ICDD's Powder Diffraction File™ (PDF®). Figure 2 illustrates the need to provide an experimental pattern at room temperature, useful for phase ID. As can be seen, the differences between the pattern recorded at room temperature and the pattern calculated from the single crystal data registered at 123 K make it difficult to properly identify bosentan monohydrate from powder data collected under normal laboratory conditions.

Given the importance that hydrogen bonding and other intermolecular interactions have on the use and performance of pharmaceutical compounds, an analysis of hydrogen bonds, C–H... π , and π ... π interactions, combined with Hirshfeld surface analysis, energy frameworks calculations, and hydrate analysis, is also presented.

II. EXPERIMENTAL METHODS

A small portion of the sample, provided by Tecnoquímicas (Cali, Colombia), was ground and mounted on a zero-background holder. The X-ray powder diffraction data were registered at room temperature with a BRUKER D8 ADVANCE diffractometer working in the Bragg-Brentano geometry. This instrument is equipped with a Cu $K\alpha$ source, working at 40 kV and 30 mA, and a LynxEye detector. The pattern was recorded from 5.00 to 60.00° in steps of 0.01526° (2 θ) at 1 s per step. The standard instrument settings (Ni filter of 0.02 mm, primary and secondary Soller slits of 2.5°, divergence slit of 0.2 mm, scatter screen height of 3 mm) were used.

III. CALCULATIONS AND COMPUTATIONAL STUDIES

The analysis of hydrogen bonds, C–H... π , and π ... π interactions was carried out with PLATON (Spek, 2020) and Mercury (Macrae et al., 2020). Hirshfeld surface analysis, “fingerprint plots”, and energy frameworks calculations (Spackman and Jayatilaka, 2009) were performed with CrystalExplorer21 (Spackman et al., 2021). The energy frameworks were calculated using the molecular wavefunction at the B3LYP/6-31G(d,p) level, within a radius of 3.8 Å, and

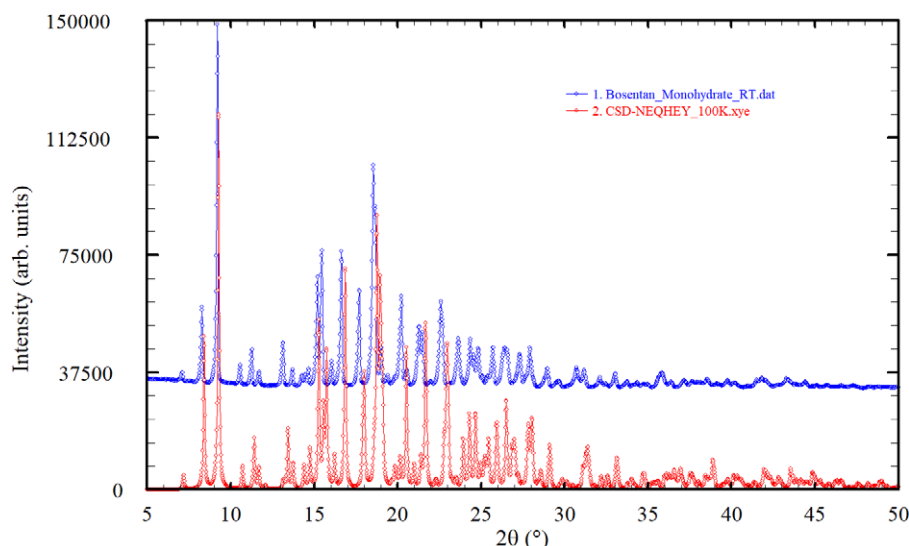


Figure 2. Comparison of the powder pattern recorded in the present study (room temperature) with the pattern calculated from single crystal data at 123 K (CSD Refcode NEQHEY, Kaur et al., 2013).

neighboring molecules within this shell were generated by symmetry operations. The space-filling environment and the interaction preferences of the water molecule in the structure were studied with the hydrate analyzer tool implemented in Mercury (Macrae et al., 2020).

IV. RESULTS AND DISCUSSION

A. Indexing and pattern fitting

The indexing of the recorded pattern carried out with DICVOL14 (Louër and Boulton, 2014), as implemented in the PreDICT graphical user interface (Blanton et al., 2019), using the first 20 peaks of the pattern produced a monoclinic unit cell with unit cell parameters: $a = 12.418(5) \text{ \AA}$, $b = 15.067(5) \text{ \AA}$, $c = 15.058(6) \text{ \AA}$, $\beta = 95.08(4)^\circ$, $V = 2806.35 \text{ \AA}^3$. This cell accounted for the 77 diffraction maxima registered. The de Wolff (de Wolff, 1968) and Smith–Snyder (Smith and Snyder, 1979) figures of merit obtained were $M_{20} = 27.7$ and $F_{20} = 95.9$ (0.0052, 40), respectively. It must be noted that the unit cell with the highest figures of merit, obtained with CONOGRAPH (Esmaili et al., 2017) using the first 30 peaks, was similar to the cell obtained with DICVOL14. The figures of merit obtained with CONOGRAPH were $M_{30} = 21.162$, $M_{30}^{\text{Wu}} = 20.279$, $M_{30}^{\text{Rev}} = 3.328$, $M_{30}^{\text{Sym}} = 70.424$, $\text{NN} = 78$, and number of solutions = 4 (Oishi-Tomiyasu, 2013). The unit cell parameters obtained agree with the values reported by Kaur et al. (2013) and by Sidoryk et al. (2014), indicating that the material under study corresponds to the reported phase of bosentan monohydrate.

The powder pattern recorded has been submitted to the ICDD through the GiA program to be incorporated into the Powder Diffraction File™ (PDF®). For this submission, integrated intensities were obtained by Le Bail refinement (Le Bail et al., 1988) using the FULLPROF software (Rodriguez-Carvajal, 1990). Weak reflections with intensities less than 0.5% of the maximum intensity were omitted. The refinement led to the following unit cell parameters: $a = 12.4520(7) \text{ \AA}$, $b = 15.110(1) \text{ \AA}$, $c = 15.0849(9) \text{ \AA}$, $\beta = 95.119(5)^\circ$, $V = 2827.0(3) \text{ \AA}^3$.

The powder patterns reported in the patents (Mathad et al., 2011; Andretto et al., 2011; Cotarca et al., 2011; Sidoryk et al., 2014; Teksin and Yilmaz Usta, 2020), digitized using the online JADE® Pattern Digitizer (ICDD, 2022), and the pattern recorded in the present work are shown in Figure 3. All the patterns are similar, indicating that they correspond to the same monohydrated phase.

A Pawley fit (Pawley, 1981) of the recorded pattern was carried out by modeling the background, sample displacement errors, absorption, cell parameters, and peak shape parameters (including anisotropic broadening) using TOPAS-Academic (Coelho, 2018). The background was modeled by a 15-term Chebyshev polynomial. The intermediate Gaussian–Lorentzian function was used with a correction for axial divergence as proposed by the program. The Pawley refinement produced a good fitting of all the diffraction maxima recorded with residuals $R_p = 0.0173$, $R_{wp} = 0.0237$, and $\text{GoF} = 1.932$, once again confirming that the unit cell was correct and the single-phase nature of the material under investigation. The analysis of the reflection conditions implemented in the CONOGRAPH software suggested $P2_1/c$ as the possible space group. This space group was also suggested by the Bayesian extinction symbol algorithm in DASH 4.0.0 (Markvardsen et al., 2001) and by DAJUST (Vallcorba et al., 2012).

An initial molecular model from the CIF file containing the structural data obtained at 100 K, reported in CSD entry NEQHEY01 (Trzcińska et al., 2016) was used for Rietveld refinement carried out with TOPAS-Academic (Coelho, 2018). The refinement included an overall scale parameter, background, sample displacement correction, peak shapes (including anisotropic broadening), unit cell parameters, absorption correction, atomic coordinates, four B_{iso} parameters, and a March–Dollase parameter. The bond distances and angles were restrained based on the values suggested by Mogul Check Geometry (Bruno et al., 2004). Four planar restraints for the molecule with a standard deviation of 0.01 \AA were also established. The isotropic atomic displacement parameters for the hydrogen atoms were 1.2 times the parameter of the C, N, or O atom to which they are attached.

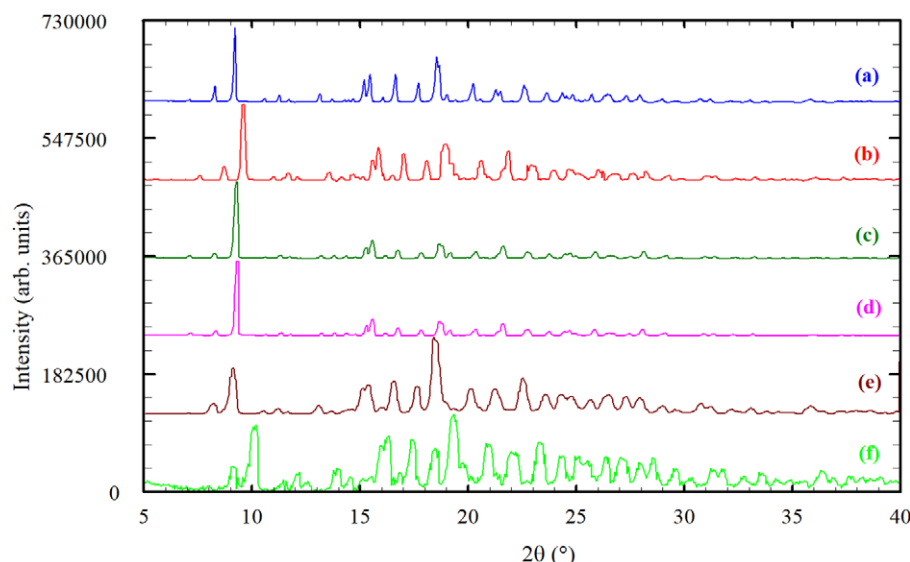


Figure 3. Comparison of the powder pattern recorded in the present study (a) for Bosentan monohydrate ($\text{BSN} \cdot \text{H}_2\text{O}$) with the reported powder patterns from the patents: (b) Mathad et al., 2011; (c) Andretto et al., 2011; (d) Cotarca et al., 2011; (e) Sidoryk et al., 2014; (f) Teksin and Yilmaz Usta, 2020.

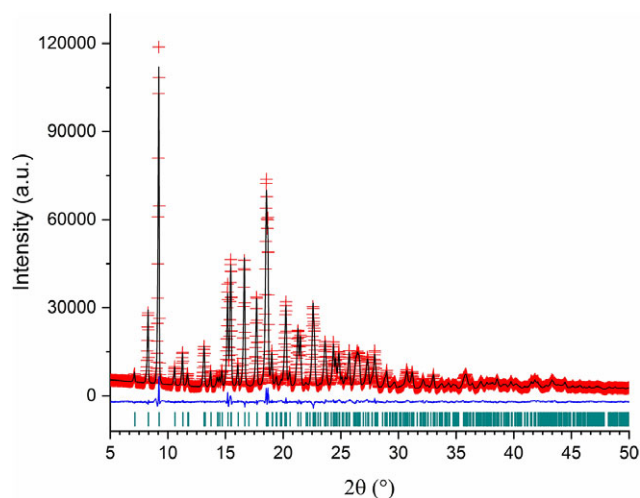


Figure 4. Rietveld refinement plot for Bosentan-H₂O.

The refinement performed with TOPAS-Academic (Coelho, 2018) was very stable. Figure 4 shows the final Rietveld refinement plot. The refinement included 277 parameters, 2012 data points (502 reflections), 197 restraints, and 4 constraints. The final whole pattern fitting converged with good figures of merit: $R_e = 0.0150$, $R_p = 0.0287$, $R_{wp} = 0.0355$, and $GoF = 2.371$. The March–Dollase preferred orientation parameter in the (1 1 0) plane was 0.923(4).

B. A closer look at the molecular structure, hydrogen bonding, C–H⋯π, and π⋯π interactions

The molecular structure of BSN-H₂O with the labeling scheme for atoms and rings is presented in Figure 5 drawn with Diamond 5.0 (Putz and Brandenburg, 2023). Bond distances and angles and torsion angles are collected in Supplementary Tables S1–S3. Their values are in agreement with the distances and angles previously reported. The comparison of the refined structure with the CSD entries NEQHEY and NEQHEY01, using the Packing Similarity feature implemented in Mercury

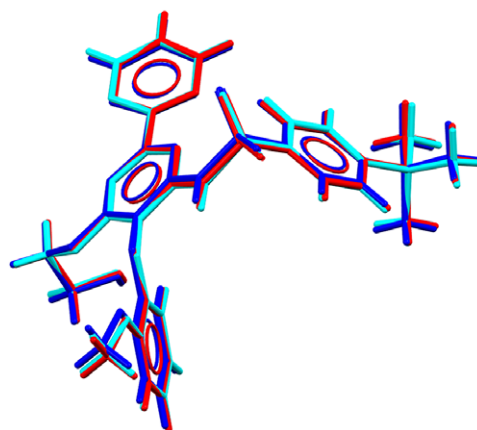


Figure 6. Superposition of the molecule of Bosentan obtained in this work (cyan) with the molecule from CSD entries NEQHEY (red) and NEQHEY01 (blue).

(Macrae et al., 2020) led to RMSCD values of 0.0790 and 0.090 Å, respectively (0.0728 and 0.0806, respectively, if using the Molecular Similarity feature). A superposition of the molecules from this study with those reported in the CSD is presented in Figure 6.

The molecule of bosentan adopts a bent conformation. Important torsion angles (Supplementary Table S3) are N1–C11–C12–O3 [−4.1(9)°], C1–S1–N1–C11 [−74.2(6)°], and C12–O3–C19–C20 [−176.5(6)°]. The planes of the pyrimidine rings, represented by B and C in Figure 5, make an angle of 28.7(3)°. Ring A is twisted by 69.8(3)° and 42.9(3)° with respect to rings B and C, respectively. Ring D makes angles of 68.0(3)° and 83.4(3)° with rings B and C, respectively.

The bent conformation of bosentan provides the appropriate geometry for several intramolecular interactions. The analysis, carried out with PLATON (Spek, 2020), indicates that there are five intramolecular N–H⋯O, O–H⋯O, C–H⋯O, and C–H⋯N hydrogen bonds involving the water molecule and the bosentan moiety. In addition, five

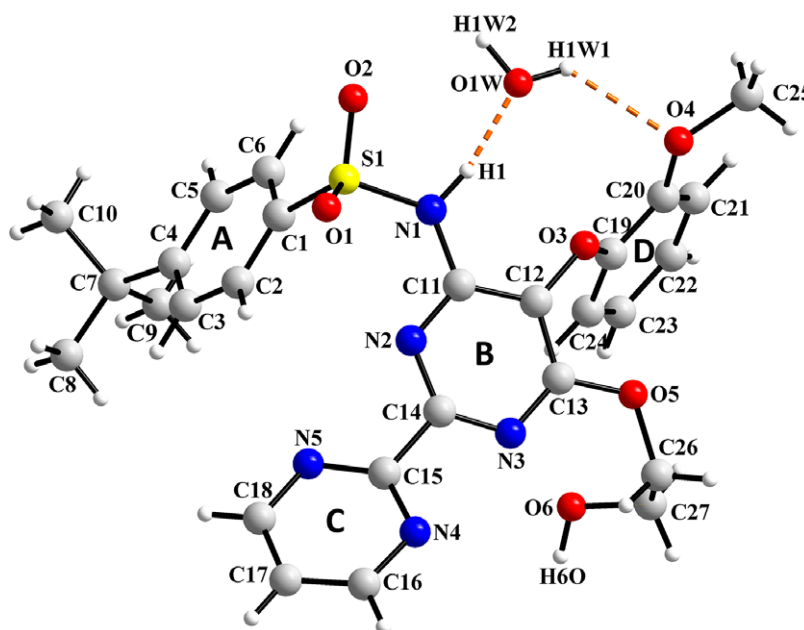


Figure 5. Molecular structure of Bosentan-H₂O with the labeling scheme for atoms and rings.

TABLE I. Hydrogen bond geometry (Å, °) for Bosentan-H₂O.

Donor—H	Acceptor	D—H	H...A	D...A	D—H...A	Symmetry
N1—H1...	O1W	0.951(12)	1.802(13)	2.738(8)	167.4(11)	.
N1—H1...	O3	0.951(12)	2.430(13)	2.799(8)	102.8(9)	.
O6—H6O...	O6	0.947(12)	2.453(14)	2.785(9)	100.5(10)	2 - x, 1 - y, 1 - z
O6—H6O...	N3	0.947(12)	2.440(12)	3.379(9)	171.5(12)	2 - x, 1 - y, 1 - z
O1W—H1W1...	O4	0.947(12)	2.332(14)	3.032(9)	130.3(11)	.
O1W—H1W2...	N4	0.944(11)	1.964(12)	2.895(9)	168.3(14)	x, 1/2 - y, 1/2 + z
C6—H6...	O2	0.949(11)	2.471(13)	2.852(9)	103.9(9)	.
C26—H26A...	N3	0.951(11)	2.358(12)	2.756(8)	104.6(8)	.
C17—H17...	O1	0.945(11)	2.394(12)	3.143(10)	136.0(8)	1 - x, 1 - y, 1 - z
C18—H18...	O2	0.952(11)	2.416(13)	3.320(11)	158.4(9)	1 - x, 1/2 + y, 3/2 - z

intermolecular hydrogen bonds occur involving O—H...O, O—H...N, and C—H...O interactions between molecules related by the *c*-glide perpendicular to [010]. Some of the hydrogen bonds reported herein are similar to those reported by Kaur et al. (2013) for NEQHEY in their single crystal study at 123 K. Table I contains the geometrical parameters for the hydrogen bonds depicted in Figure 7a,b.

In addition to extensive hydrogen bonding, C—H... π , and π ... π interactions play a role in stabilizing the structure. The geometric parameters of these interactions are presented in Table II. The strongest π ... π contact (shown in Figure 7c) occurs between the centroids of rings *C* of two bosentan molecules related by inversion. The centroid-to-centroid (CgC—CgC) distance is 3.563(4) Å. At the same time, the C27—H27B end of two neighboring molecules participate in C—H... π interactions with the two CgC in contact by π ... π interactions, at distances of 2.995(10) Å.

A view of the structure of BSN-H₂O is shown in Figure 8. The structure can be described in terms of columns of bosentan and water molecules that run along the *c*-axis and pack along the *a*-axis joined by hydrogen bonds where only bosentan molecules participate.

C. Hirshfeld surface analysis, energy frameworks calculations, and hydrate analysis

The Hirshfeld surface (HS), calculated with *CrystalExplorer*21.5 (Spackman et al., 2021), provides useful tools for the analysis and representation of intermolecular contacts. Figure 9 depicts the HS mapped onto several functions for the BSN and the water moieties: d_{norm} (a,d), shape index (b,e), and curvedness (c,f). In Figure 9a,d, the red spots represent the intermolecular contacts shorter than the sum of van der Waals radii, while the longest contacts are represented in blue. The indentations where the red spots occur indicate the points of contact of the water molecule. The HS analysis reveals that the most important intermolecular interactions correspond, as expected, to the hydrogen bonds between the BSN and the water molecules. In the shape index function mapped on the HS (shown in Figure 9b,e) the blue bumps and the red-orange dents indicate where interactions occur. The bosentan and water molecules are arranged along the *b*-axis next to each other, in an alternating fashion, with the BSN shape index dents being complementary to the water shape index bumps (Figure 9b,e). The interactions between the *C* aromatic rings appear as triangular spots on the map of the shape index and correspond to the π ... π interactions described in the previous section, summarized in Table II. The curvedness function for

the BSN molecule (Figure 9c,f) displays flat areas, the most relevant of them located on the *C* ring where the π ... π interactions take place. The curvedness function mapped for the water molecule (Figure 9f) is characterized by flat faces where the bosentan molecule is “anchored” through the hydrogen bonds. These contacts contribute to the crystal packing of the material in layers of alternating BSN and water molecules (Figure 9g).

The “fingerprint plots” (Figure 10) representing distances of intermolecular interactions (Spackman and Jayatilaka, 2009) provide additional insight into the contributions of such interactions. Figure 10a (for bosentan) and Figure 10k (for water) represent all interactions in which these two moieties are involved. In the subsequent diagrams the contributions of each contact are plotted. They indicate that, in bosentan, the most important contacts are H...H, C...H/H...C, and O...H/H...O, contributing 43.8, 22.3, and 22.1%, respectively. H...N/N...H contacts represent a 9.3% while other interactions contribute less than 1%. For the water molecule, the O...H/H...O contact represents 48.4%, the H...H a 38.3%, and the H...N/N...H a 12.1%.

The structure of bosentan monohydrate is densely packed. The volume of the HS for the bosentan molecule is 664.70 Å³ and 24.27 Å³ for the water molecule, corresponding to a total volume of 688.97 Å³, which represents 98.26% of the volume of the unit cell.

The analysis of the space occupied by the water molecules and their interactions with the closest neighbors was carried out using the hydrate analyzer tool incorporated in Mercury (Macrae et al., 2020), and the graphical representation is shown in Figure 11. The water molecules occupy 59.51 Å³, representing 2.1% of the volume of the unit cell. Each water molecule is hydrogen bonded to two bosentan molecules and each bosentan binds to two water molecules. They arrange in double layers parallel to the *bc*-plane and stack along the *a*-axis connected by hydrogen bonds between bosentan moieties (Figure 11a). The interaction maps for the water probe are shown in Figure 11b. The greatest number of interactions are observed in the contours with the most intense color levels. The most important interactions of the water molecule are with the O3 and O4 oxygen atoms from ring *D* (magenta outline), with the hydroxyl group (orange circle) and with N3 from ring *B* (green ellipse). As can be seen, in the packing, the water molecules interact with almost the entire bosentan molecule.

The interaction energies between the central molecule and neighboring molecules within a radius of 3.8 Å are shown

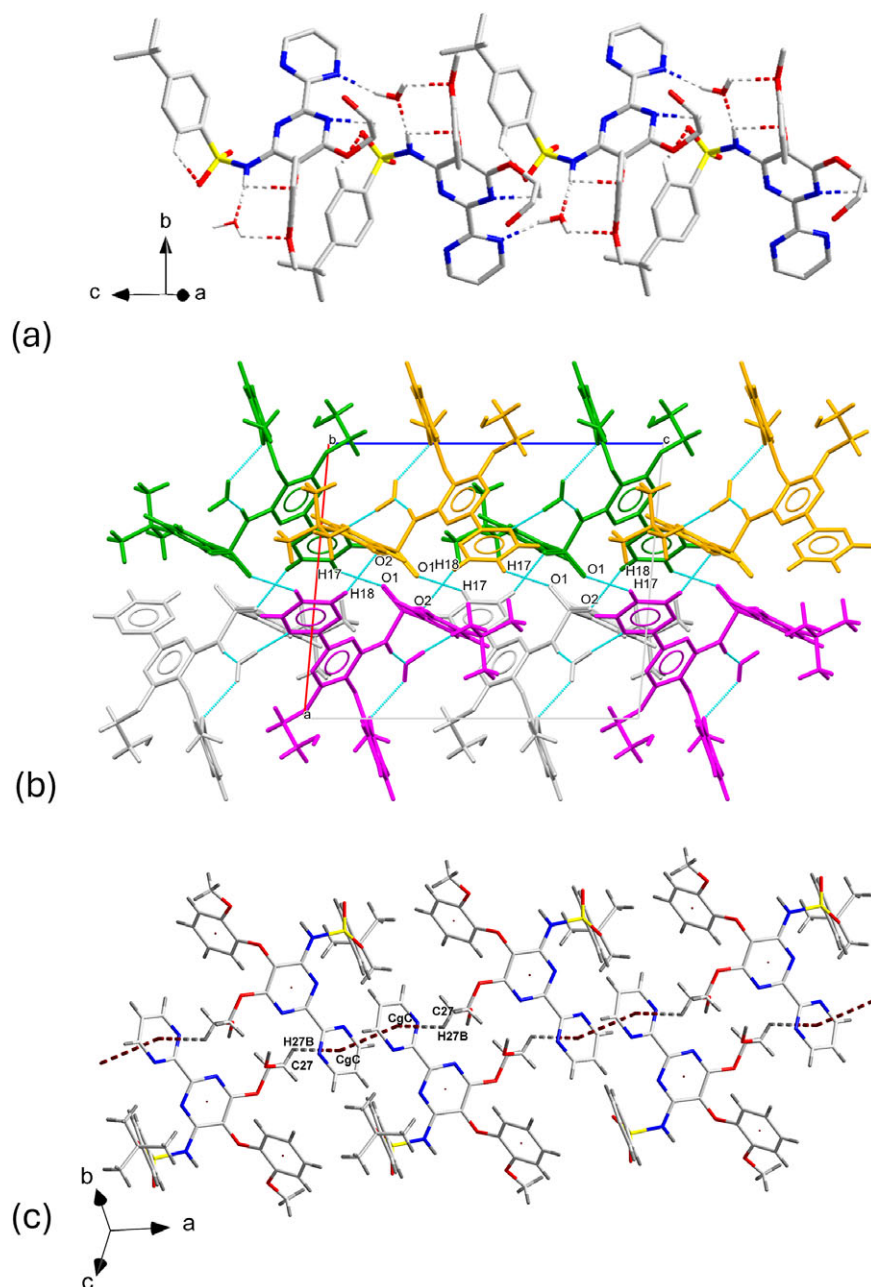


Figure 7. (a) Partial view of the chains of hydrogen bonded molecules related by a c -glide along the c -axis; (b) chains connected via hydrogen bonding; color scheme: (i) x, y, z in light grey; (ii) $-x, 1/2 + y, 1/2 - z$ in green; (iii) $-x, -y, -z$ in gold; (iv) $x, 1/2 - y, 1/2 + z$ in magenta; (c) sequence of molecules connected by one $C-H\cdots\pi$ and the $\pi\cdots\pi$ interactions.

TABLE II. Geometry of $C-H\cdots\pi$, and $\pi\cdots\pi$ interactions in Bosentan- H_2O .

$C-H\cdots\pi$	$H\cdots Cg(\pi)$ (Å)	$H-Perp$ (Å)	γ (°)	$C-H\cdots Cg(\pi)$ (°)	Symmetry
$C27-H27B\cdots Cg(C)$	2.995(10)	2.81	20.15	113.8(7)	$2-x, 1-y, 1-z$
$C6-H6\cdots Cg(B)$	2.836(11)	-2.75	14.53	144.4(8)	$x, 1/2-y, 1/2+z$
$C10-H10A\cdots Cg(A)$	2.964(9)	-2.78	20.20	147.3(8)	$1-x, 1-y, 2-z$
$C26-H26B\cdots Cg(D)$	2.856(10)	2.85	4.68	135.9(7)	$x, 1/2-y, -1/2+z$
$\pi\cdots\pi$	d (Å)	$\alpha/\beta/\gamma$ (°)	$Cg(C)_{Perp}/Cg(C)^i_{Perp}$ (Å)	Slippage (Å)	
$Cg(C)\cdots Cg(C)^i$	3.563(4)	0.0(3)/19.6/19.6	3.357(3)/3.357(3)	1.195	$1-x, 1-y, 1-z$

$Cg(\pi)$ denotes the centroids $Cg(A)$, $Cg(B)$, $Cg(C)$, and $Cg(D)$ of rings **A**, **B**, **C**, and **D** (π -rings) respectively, as depicted in Figure 5. The geometry of the contacts is defined in PLATON [Spek, 2020] by the following parameters: $H-Perp$ = perpendicular distance of H to the plane of rings **A**, **B**, **C**, or **D** (Figure 5); γ = angle between the $Cg(\pi)-H$ or the $Cg(C)-Cg(C)^i$ vector and the normal to plane **C**; $d = Cg(C)\cdots Cg(C)^i$ distance; α = dihedral angle between Planes **C** and C^i ; β = angle between the $Cg(C)-Cg(C)^i$ vector and the normal to plane **C**; $Cg(C)_{Perp}$ = perpendicular distance of $Cg(C)$ on ring C^i ; $Cg(C)^i_{Perp}$ = Perpendicular distance of $Cg(C)^i$ on ring **C**; **Slippage** = distance between $Cg(C)$ and the perpendicular projection of $Cg(C)^i$ on ring **C**. The symmetry operation $1-x, 1-y, 1-z$ is denoted by the superscript i .

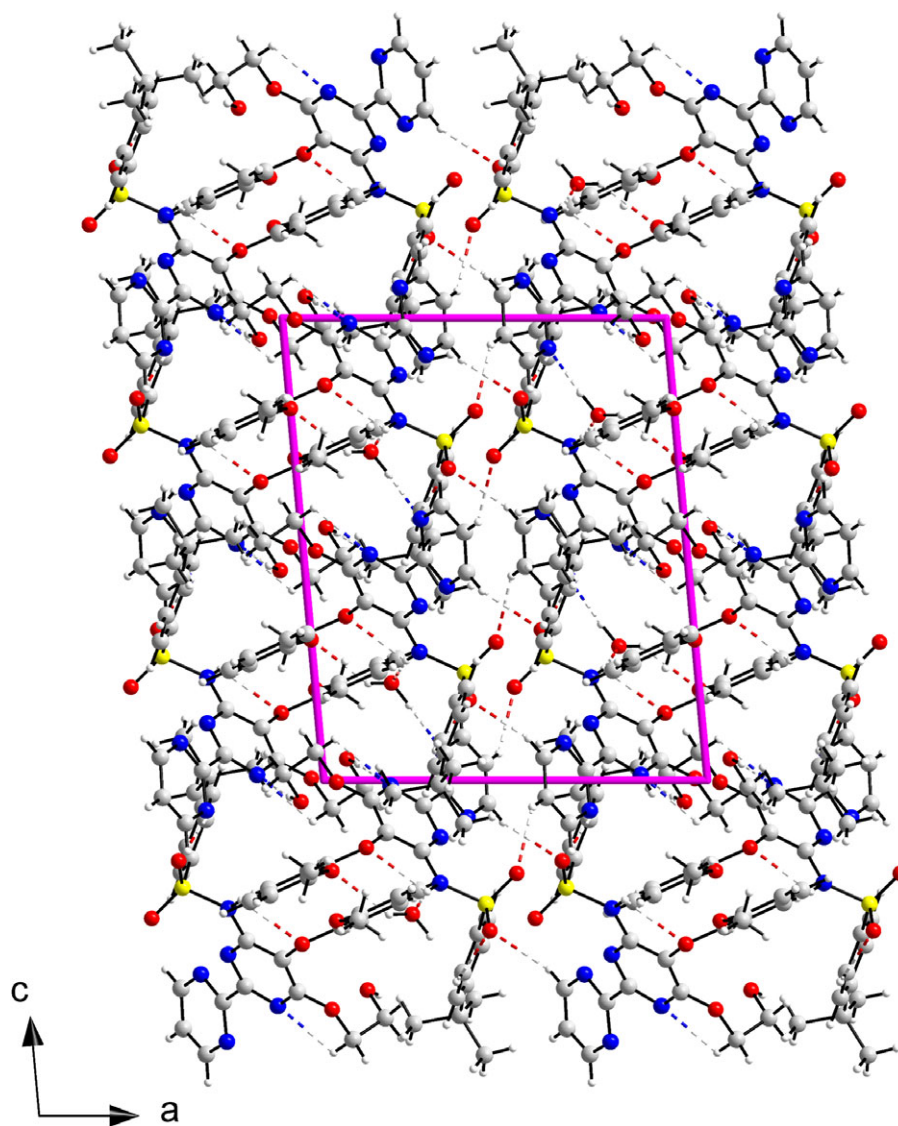


Figure 8. Crystal structure of Bosentan-H₂O viewed down the *b*-axis.

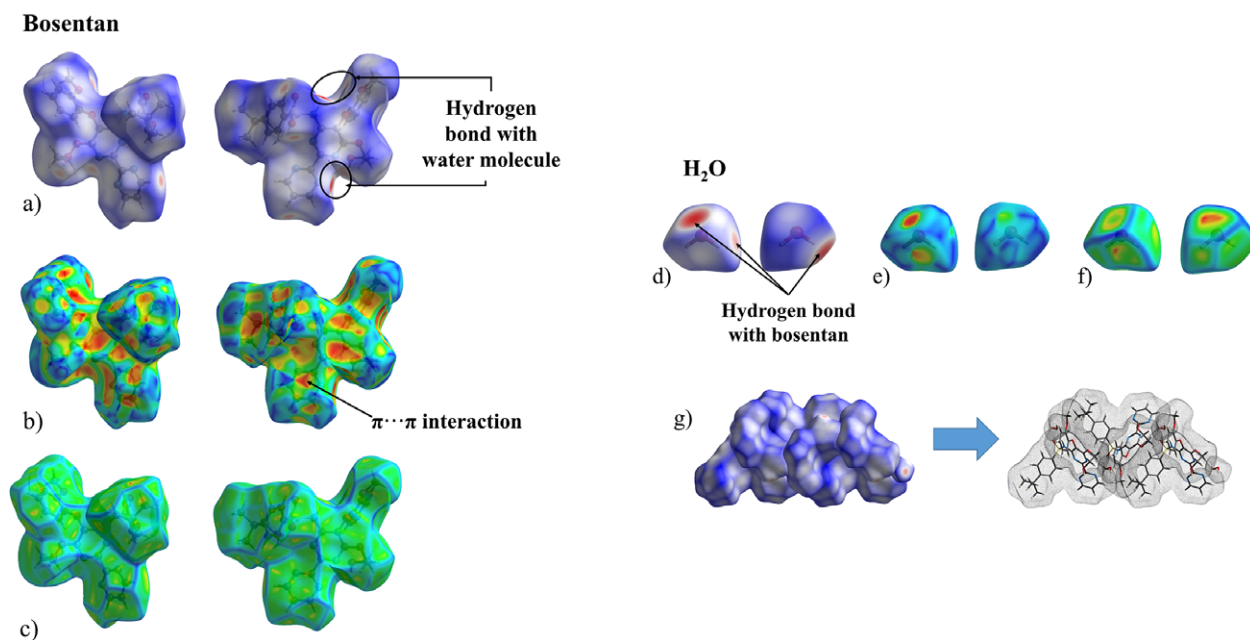


Figure 9. Hirshfeld surface mapped onto d_{norm} shape index, and curvedness for the Bosentan molecule (a, b, c, respectively) and the H₂O molecule (d, e, f, respectively) in Bosentan-H₂O; g depicts the packing of Bosentan and water molecules.

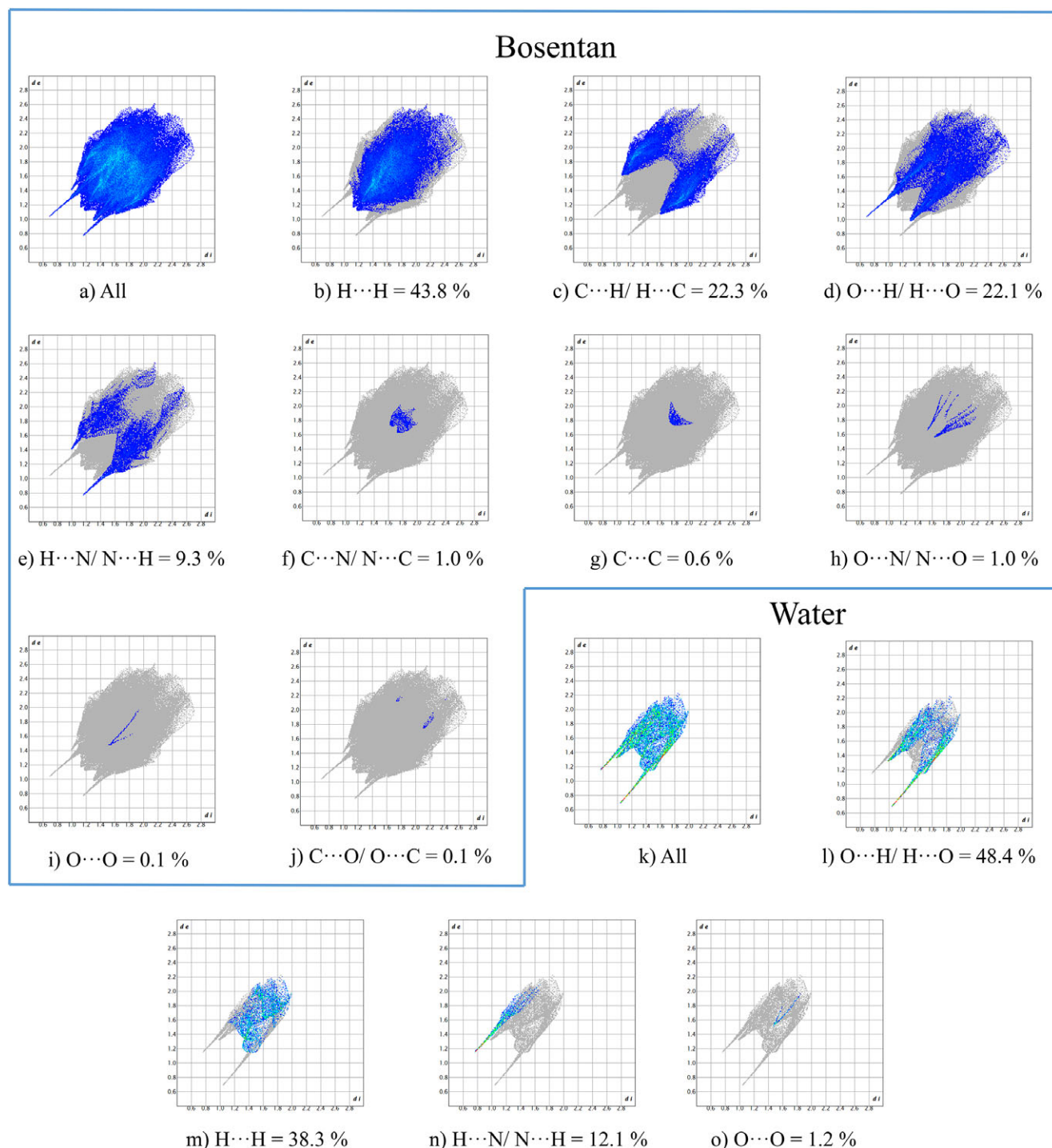


Figure 10. Fingerprint plots for the Bosentan molecule (a–j) and for the water molecule (k–o) with percent contributions from specific pairs of interatomic interactions.

in [Supplementary Table S4](#). The highest stabilization interaction energies are observed between BSN molecules related by inversion ($E_{\text{tot}} = -84.1$ kJ/mol and -64.1 kJ/mol), followed by interactions of neighboring molecules with symmetry operation $-x, y + 1/2, -z + 1/2$ ($E_{\text{tot}} = -51.5$ kJ/mol) and the units related by $x, -y + 1/2, z + 1/2$ ($E_{\text{tot}} = -39.7$ kJ/mol). The most relevant BSN interactions with the water molecule have energy values of -45.0 kJ/mol and -32.3 kJ/mol, corresponding to the hydrogen bonds $\text{O1W}\cdots\text{H1}$ and $\text{N4}\cdots\text{H1W2}$. The topology of the energy frameworks ([Figure 12](#)) shows that the -84.1 kJ/mol interaction extends

along the c -axis forming chains that are connected parallel to the a -axis by contacts with energies of -64.1 kJ/mol and -33.0 J/mol while the interactions between BSN and water extend in a zigzag fashion along the c -axis.

V. DEPOSITED DATA

Crystallographic information framework (CIF) files containing the results of the Rietveld refinement and a CIF with the data submitted for the GiA program were deposited with the ICDD (Editorial Number G000465). The data can be

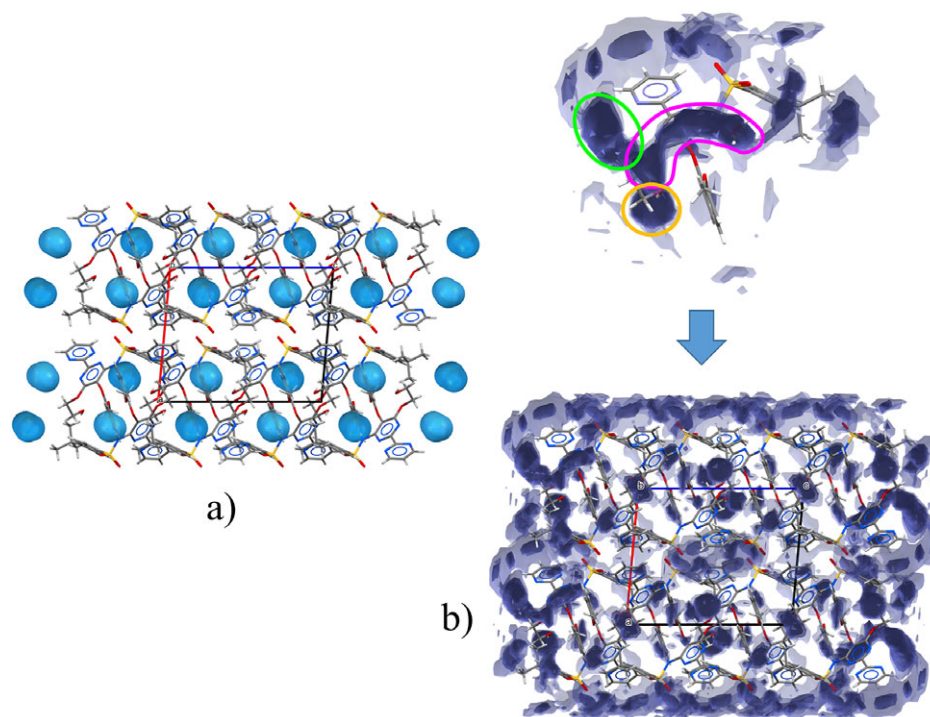


Figure 11. (a) View down the *b*-axis of the volume occupied by the water molecules calculated using the hydrate analyzer tool in Mercury (Macrae et al., 2020) and (b) interaction map for the water molecules in Bosentan·H₂O.

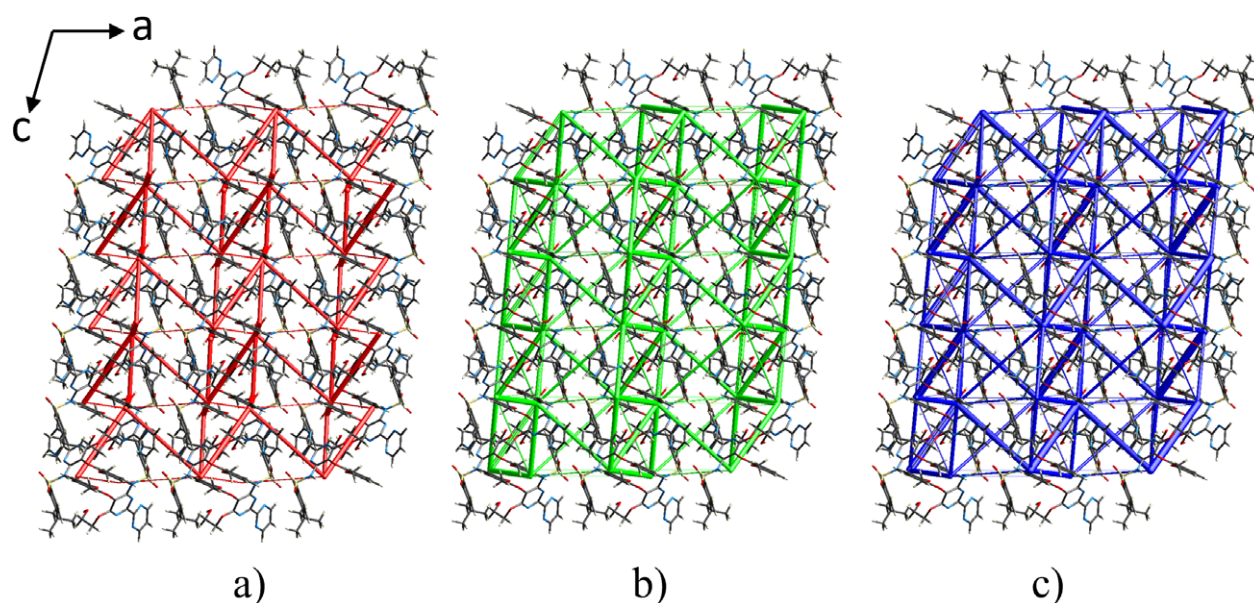


Figure 12. Energy frameworks for Bosentan·H₂O calculated with *CrystalExplorer* (Spackman et al., 2021) viewed down the *b*-axis. (a) electrostatic, E_{ele} , red; (b) dispersive, E_{disp} , green; (c) total energy, E_{tot} , blue. The cylinder radii were scaled to 75 arbitrary units and the energy cutoff is 5 kJ mol⁻¹.

requested at pdj@icdd.com. The crystal structure data were also deposited with the Cambridge Crystallographic Data Centre (CCDC 2372331).

SUPPLEMENTARY MATERIAL

To view supplementary material for this article, please visit <http://doi.org/10.1017/S0885715625000065>.

ACKNOWLEDGMENTS

The authors thank the support of Vicerrectoría de Investigación y Extensión de Universidad Industrial de Santander (UIS), Colombia. Access to the Cambridge Structural Database for Universidad de Los Andes (Venezuela) was possible through the *Frank H. Allen International Research & Education Programme* (FAIRE) from the Cambridge Crystallographic Data Centre.

CONFLICTS OF INTEREST

The authors declare no competing interests.

REFERENCES

- Andretto, M., C. Colli, L. Cotarca, P. Maragni, A. Melloni, E. Melotto, I. Michieletto, M. Verzini, and R. Volpicelli. 2011. "Process for Preparing Bosentan Monohydrate and its Intermediates." Patent Assignee Zach System SpA, Application No. 2011310754, Patent AU2011310754B2, 22 September 2011. <https://patents.google.com/patent/AU2011310754B2/en>.
- Barbas, R., A. Portell, C. A. Hunter, R. Prohens, and A. Frontera. 2022. "Combined Computational/Experimental Investigation of New Cocrystals of the Drug Bosentan." *CrystEngComm* 24: 5105–5111. <https://doi.org/10.1039/D2CE00581F>.
- Blanton, J. R., R. J. Papoular, and D. Louër. 2019. "PreDICT: A Graphical User Interface to the DICVOL14 Indexing Software Program for Powder Diffraction Data." *Powder Diffraction* 34 (3): 233–241. <https://doi.org/10.1017/S0885715619000514>.
- Bruno, I. J., J. C. Cole, M. Kessler, J. Luo, W. D. S. Motherwell, L. H. Purkis, B. R. Smith, R. Taylor, R. I. Cooper, S. E. Harris, and A. G. Orpen. 2004. "Retrieval of Crystallographically-Derived Molecular Geometry Information." *Journal of Chemical Information and Computer Sciences* 44 (6): 2133–2144. <https://doi.org/10.1021/ci049780b>.
- Coelho, A. A. 2018. "TOPAS and TOPAS-Academic: An Optimization Program Integrating Computer Algebra and Crystallographic Objects Written in C++." *Journal of Applied Crystallography* 51 (1): 210–218. <https://doi.org/10.1107/S1600576718000183>.
- Cotarca, L., M. Verzini, E. Melotto, I. Michieletto, A. Melloni, P. Maragni, R. Volpicelli, M. Andretto, and C. Colli. 2011. "Verfahren zur Herstellung von Bosentanmonohydrat und Zwischenprodukten Davon." Patent Assignee Zach System SpA, Application No. 11761348.9, Patent EP2621909B1, 22 September 2011. <https://patents.google.com/patent/EP2621909B1/de>.
- Dávila-Miliani, M. C., A. Dugarte-Dugarte, R. A. Toro, J. E. Contreras, H. A. Camargo, J. A. Henao, J. M. Delgado, and G. Díaz de Delgado. 2020. "Polymorphism in the Anti-Inflammatory Drug Flunixin and Its Relationship with Clonixin." *Crystall Growth & Design* 20 (7): 4657–4666. <https://doi.org/10.1021/acs.cgd.0c00284>.
- de Wolff, P. M. 1968. "A Simplified Criterion for the Reliability of a Powder Pattern Indexing." *Journal of Applied Crystallography* 1 (2): 108–113. <https://doi.org/10.1107/S002188986800508X>.
- Dugarte-Dugarte, A. J., R. A. Toro, J. van de Streek, J. A. Henao, G. Díaz de Delgado, and J. M. Delgado. 2022. "Crystal Structure from Laboratory X-Ray Powder Diffraction Data, DFT-D Calculations, and Hirshfeld Surface Analysis of (S)-Dapoxetine Hydrochloride." *Powder Diffraction* 37 (4): 216–224. <https://doi.org/10.1017/S0885715622000380>.
- Dugarte-Dugarte, A. J., R. A. Toro, J. van de Streek, J. A. Henao, A. N. Fitch, C. Dejoie, J. M. Delgado, and G. Díaz de Delgado. 2023. "Hydrogen Bonding Patterns and C–H... π Interactions in the Structure of the Antiparkinsonian Drug (R)-Rasagiline Mesylate Determined Using Laboratory and Synchrotron X-Ray Powder Diffraction Data." *Acta Crystallographica Section B. Structural Science, Crystal Engineering and Materials* 79 (6): 462–472. <https://doi.org/10.1107/S2052520623007758>.
- Easwaramoorthi, K., A. J. Rajendran, K. C. Rao, Y. Arun, C. Balachandran, P. T. Perumal, E. Nobuhiko, S. M. Mahalingam, V. Duraipandian, and N. A. Al-Dhabi. 2015. "Synthesis of Novel 1,4-Disubstituted 1,2,3-Triazolo-Bosentan Derivatives – Evaluation of Antimicrobial and Anticancer Activities and Molecular Docking." *RSC Advances* 5: 105266–105278. <https://doi.org/10.1039/C5RA18618H>.
- Enevoldsen, F. C., J. Sahana, M. Wehland, D. Grimm, M. Infanger, and M. Krüger. 2020. "Endothelin Receptor Antagonists: Status Quo and Future Perspectives for Targeted Therapy." *Journal of Clinical Medicine* 9 (3): 824. <https://doi.org/10.3390/jcm9030824>.
- Esmaili, A., T. Kamiyama, and R. Oishi-Tomiyasu. 2017. "New Functions and Graphical User Interface Attached to Powder Indexing Software CONOGRAPH." *Journal of Applied Crystallography* 50 (2): 651–659. <https://doi.org/10.1107/S1600576717001145>.
- Giménez, V. M., N. Sperandeo, S. Faudone, S. Noriega, W. Manucha, and D. Kassuha. 2019. "Preparation and Characterization of Bosentan Monohydrate/E-Polycaprolactone Nanoparticles Obtained by Electrospraying." *Biotechnology Progress* 35 (2): e2748. <https://doi.org/10.1002/btpr.2748>.
- Groom, C. R., I. J. Bruno, M. P. Lightfoot, and S. C. Ward. 2016. "The Cambridge Structural Database." *Acta Crystallographica Section B. Structural Science, Crystal Engineering and Materials* 72 (2): 171–179. <https://doi.org/10.1107/S2052520616003954>.
- ICDD. 2022. JADE® Pattern Digitizer. <https://www.icdd.com/jade-pattern-digitizer/?page=www.icdd.com/JadeSAS/jade-pattern-digitizer/>. Accessed May 4, 2024.
- Jadhav, P., and Y. Pore. 2017. "Physicochemical, Thermodynamic and Analytical Studies on Binary and Ternary Inclusion Complexes of Bosentan with Hydroxypropyl- β -Cyclodextrin." *Bulletin of Faculty of Pharmacy, Cairo University* 55 (1): 147–154. <https://doi.org/10.1016/j.bfopcu.2016.12.004>.
- Kabekkodu, S. N., A. Dosen, and T. N. Blanton. 2024. "PDF-5+; A Comprehensive Powder Diffraction File™ for Materials Characterization." *Powder Diffraction*, 39 (2): 47–59. <https://doi.org/10.1017/S0885715624000150>.
- Kaur, M., J. P. Jasinski, A. C. Keeley, H. S. Yathirajan, R. Betz, T. Gerber, and R. J. Butcher. 2013. "Bosentan Monohydrate." *Acta Crystallographica Section E. Crystallographic Communications* 69 (1): o12–o13. <https://doi.org/10.1107/S1600536812048969>.
- Khandar, A. A., Z. Mirzaei-Kalar, J. M. White, S. A. Hosseini-Yazdi, A. Kebriaeezadeh, and A. Jouyban. 2017. "Solubility, Potentiometric and Thermodynamic Studies on Zinc-Bosentan Complex; Synthesis and X-Ray Crystal Structure." *Journal of Molecular Liquids* 234: 64–72. <https://doi.org/10.1016/j.molliq.2017.03.046>.
- Krupa, A., F. Danède, A. Węgrzyn, D. Majda, and J.-F. Willart. 2022. "Thinking of Bosentan Repurposing – A Study on Dehydration and Amorphization." *International Journal of Pharmaceutics* 622: 21846. <https://doi.org/10.1016/j.ijpharm.2022.121846>.
- Łaszc, M., A. B. Witkowska, K. Trzcńska, M. Kubiszewski, and K. Kuziak. 2012. "Analiza Wodzianów Substancji Czynnych. (Analysis of Pharmaceutical Hydrates) *Przemysł Chemiczny* 91: 333–341.
- Le Bail, A., H. Duroy, and J. L. Fourquet. 1988. "Ab-Initio Structure Determination of LiSbWO₆ by X-Ray Powder Diffraction." *Materials Research Bulletin* 23 (3): 447–452. [https://doi.org/10.1016/0025-5408\(88\)90019-0](https://doi.org/10.1016/0025-5408(88)90019-0).
- Lee, H., J. Kang, H. Lee, D. Kim, Y. Rhee, J. Kim, E. Park, and C. Park. 2016. "Preparation and Physicochemical Characterization of Spray-Dried and Jet-Milled Microparticles Containing Bosentan Hydrate for Dry Powder Inhalation Aerosols." *Drug Design, Development and Therapy* 10: 4017–4030. <https://doi.org/10.2147/DDDT.S120356>.
- Louër, D., and A. Boulton. 2014. "Some Further Considerations in Powder Diffraction Pattern Indexing with the Dichotomy Method." *Powder Diffraction* 29(S2): S7–S12. <https://doi.org/10.1017/S0885715614000906>.
- Macrae, C. F., I. Sovago, S. J. Cottrell, P. T. A. Galek, P. McCabe, E. Pidcock, M. Platings, G. P. Shields, J. S. Stevens, M. Towler, and P. A. Wood. 2020. "Mercury 4.0: From Visualization to Analysis, Design and Prediction." *Journal of Applied Crystallography* 53 (1): 226–235. <https://doi.org/10.1107/S1600576719014092>.
- Markvardsen, A. J., W. I. F. David, J. C. Johnson, and K. Shankland. 2001. "A Probabilistic Approach to Space-Group Determination from Powder Diffraction Data." *Acta Crystallographica Section A. Foundations and Advances* 57 (1): 47–54. <https://doi.org/10.1107/S0108767300012174>.
- Mathad, V. T., N. C. Niphade, K. M. Jagtap, and C. T. Gaikwad. 2011. "Process for Preparation of Bosentan." Patent Assignee Megafine Pharma P Ltd, Application No. 13/816,376, Patent US9139537B2, 28 March 2011. <https://patents.google.com/patent/US9139537B2/en>.
- Mathier, M. A., and D. Ishizawa. 2010. "Bosentan." *Expert Opinion on Pharmacotherapy*. 11 (6): 1023–1034. <https://doi.org/10.1517/14656561003691854>.
- Minecka, A., K. Chmiel, K. Jurkiewicz, B. Hachuła, R. Łunio, D. Zakowicki, K. Hyla, B. Milanowski, K. Koperwas, K. Kamiński, M. Paluch, and E. Kamińska. 2022. "Studies on the Vitrified and Cryomilled Bosentan." *Molecular Pharmaceutics* 19 (1): 80–90. <https://doi.org/10.1021/acs.molpharmaceut.1c00613>.
- Mohapatra, S., D. Dash, M. R. Bhise, A. Kandalkar, S. Vasu, S. Pahuja, and N. S. Bhajipale. 2022. "Formulation and Characterization of Polymeric Nanoparticle of Antihypertensive Drug Bosentan." *Asian Journal of Organic & Medicinal Chemistry* 7 (2) (Special Issue – II 2022): 372–379.

- Oishi-Tomiyasu, R. 2013. "Reversed de Wolff Figure of Merit and its Application to Powder Indexing Solutions" *Journal of Applied Crystallography* 46 (5), 1277–1282. <https://doi.org/10.1107/S0021889813018773>.
- Pawley, G. S. 1981. "Unit-Cell Refinement from Powder Diffraction Scans." *Journal of Applied Crystallography* 14 (6): 357–361. <https://doi.org/10.1107/S0021889881009618>.
- Putz, H. and K. Brandenburg. 2023. Diamond-Crystal and Molecular Structure Visualization, Crystal Impact-GbR, Kreuzherrenstr, Bonn, Germany 102: 53227, <https://www.crystalimpact.de/diamond>.
- Rodriguez-Carvajal, J. 1990. "FULLPROF: a Program for Rietveld Refinement and Pattern Matching Analysis." Abstracts of the Satellite Meeting on Powder Diffraction of the XV Congress of the IUCr, Toulouse, France, p. 127.
- Sagar, B. K., H. S. Yathirajan, J. P. Jasinski, and C. Glidewell. 2016. "Crystal Structure of 6-hydroxy-5-(2-methoxyphenoxy)-2,2'-bipyrimidin-4(3H)-one," *Acta Crystallographica Section E. Crystallographic Communications* 72 (7): 969–971. <https://doi.org/10.1107/S2056989016009075>.
- Sidoryk, K., W. Łuniewski, M. Puchalska, M. Łaszcz, W. Maruszak, and M. Kościuch. 2014. "Process for Preparation of Bosentan Monohydrate of Pharmaceutical Purity." Patent Assignee Instytut Farmaceutyczny, Application No. PCT/PL2013/000173, Patent WO2014104904A1, 3 July 2014. <https://patents.google.com/patent/WO2014104904A1/ru>.
- Smith, G. S., and R. L. Snyder. 1979. "FN: A Criterion for Rating Powder Diffraction Patterns and Evaluating the Reliability of Powder-Pattern Indexing." *Journal of Applied Crystallography* 12 (1): 60–65. <https://doi.org/10.1107/S002188987901178X>.
- Spackman, M. A., and D. Jayatilaka. 2009. "Hirshfeld Surface Analysis." *Crystal Engineering Communications* 11 (1): 19–32. <https://doi.org/10.1039/B818330A>.
- Spackman, P. R., M. J. Turner, J. J. McKinnon, S. K. Wolff, D. J. Grimwood, D. Jayatilaka, and M. A. Spackman. 2021. "CrystalExplorer: A Program for Hirshfeld Surface Analysis, Visualization and Quantitative Analysis of Molecular Crystals." *Journal of Applied Crystallography* 54 (3): 1006–1011. <https://doi.org/10.1107/S1600576721002910>.
- Spek, A. L. 2020. "checkCIF Validation ALERTS: What they Mean and How to Respond." *Acta Crystallographica Section E. Crystallographic Communications* 76 (1): 1–11. <https://doi.org/10.1107/S2056989019016244>.
- Teksin, Z. Ş., and D. Yilmaz Usta. 2020. "Bosentan Monohydrate Loaded Liquid Self Nanoemulsifying Drug Carrier System and Tablet Formulation." Patent Assignee Teksin, Z. Ş. and Yilmaz Usta, D. Application No. PCT/TR2020/050945, Patent WO2021076081A2, 13 October 2020. <https://patents.google.com/patent/WO2021076081A3/en>.
- Toro, R. A., A. Dugarte-Dugarte, J. van de Streek, J. A. Henao, J. M. Delgado, and G. Díaz de Delgado. 2022. "Crystal Structure from X-Ray Powder Diffraction Data, DFT-D Calculation, Hirshfeld Surface Analysis, and Energy Frameworks of (RS)-Trichlormethiazide." *Acta Crystallographica Section E. Crystallographic Communications* 78 (2): 140–148. <https://doi.org/10.1107/S2056989021013633>.
- Trzcińska, K., M. Łaszcz, and K. Sidoryk. 2016. *CSD-Refcode NEQHEY01*. Private Communication.
- Vallcorba, O., J. Rius, C. Frontera, I. Peral, and C. Miravittles. 2012. "DAJUST: A Suite of Computer Programs for Pattern Matching, Space-Group Determination and Intensity Extraction from Powder Diffraction Data." *Journal of Applied Crystallography* 45 (4): 844–848. <https://doi.org/10.1107/S0021889812021152>.